



HAL
open science

Simulation of Vibrating Intrinsic Reverberation Chambers Using an FDTD Conformal Mesh

Florian Mahiddini, Guillaume Andrieu, Nicolas Bui, Christophe Guiffaut

► **To cite this version:**

Florian Mahiddini, Guillaume Andrieu, Nicolas Bui, Christophe Guiffaut. Simulation of Vibrating Intrinsic Reverberation Chambers Using an FDTD Conformal Mesh. *IEEE Transactions on Electromagnetic Compatibility*, 2023, 65 (3), pp.617 - 624. 10.1109/temc.2023.3259241 . hal-04278403

HAL Id: hal-04278403




<https://hal.science/hal-04278403v1>

Submitted on 10 Nov 2023

HAL is a multi-disciplinary open access archive for the deposit and dissemination of scientific research documents, whether they are published or not. The documents may come from teaching and research institutions in France or abroad, or from public or private research centers.

L'archive ouverte pluridisciplinaire **HAL**, est destinée au dépôt et à la diffusion de documents scientifiques de niveau recherche, publiés ou non, émanant des établissements d'enseignement et de recherche français ou étrangers, des laboratoires publics ou privés.

Simulation of Vibrating Intrinsic Reverberation Chambers Using an FDTD Conformal Mesh

Florian Mahiddini, Guillaume Andrieu , Senior Member, IEEE, Nicolas Bui ,
and Christophe Guiffaut , Member, IEEE

Abstract—This article presents an original simulation procedure devoted to the simulation of arbitrary-shaped reverberation chambers especially well suited for the analysis of vibrating intrinsic reverberation chambers (VIRC). The described method is based upon conformal finite-difference in time-domain (FDTD) modeling in order to model the rough surface geometry of the VIRC walls. On this point, we take full advantage of the performance of our in-house numerical FDTD code called TEMSI-FD and of its associated conformal mesher. First, uncorrelated geometries of the VIRC under study have been generated in order to analyze its performance as a RC from the computed S_{11} parameter of a log-periodic antenna. Second, correlated geometries have been generated in order to consider the continuous movement of the VIRC walls with a straightforward algorithm, each geometry being associated to a given instant. In both frequency and time domains, numerical outcomes demonstrate excellent agreement with experimental results available in the literature in similar conditions.

Index Terms—Conformal mesh, electromagnetic compatibility (EMC) testing, finite-difference in time-domain (FDTD), reverberation chamber (RC), S-parameter, vibrating intrinsic reverberation chamber (VIRC).

I. INTRODUCTION

REVERBERATION chambers (RC) are oversized metallic cavities providing a homogeneous and isotropic electromagnetic (EM) field if a certain number of independent configurations are considered, for instance with the use of a mechanical mode stirrer. RCs are commonly used for electromagnetic compatibility (EMC) tests but also for other applications, such as characterization of antennas, shieldings, wireless devices, or materials. For different purposes, researchers have tried over the last years to model numerically a RC with a full-wave software solving the Maxwell equations. Although it is a difficult task to handle numerically such oversized metallized cavities, different numerical techniques, such as finite-difference time-domain (FDTD) [1], [2], transmission-line matrix (TLM) [3], image theory [4], and method of moments (MoM) [5], [6], have already been proposed.

Manuscript received 12 October 2022; revised 27 January 2023; accepted 11 March 2023. Date of publication 3 April 2023; date of current version 13 June 2023. This work was supported in part by the XLIM laboratory and in part by the DGA/AID within the framework of the Project ASTRID/CHAOTIQ. (Corresponding author: Guillaume Andrieu.)

The authors are with the XLIM Laboratory, 87000 Limoges, France (e-mail: florian.mahiddini@unilim.fr; guillaume.andrieu@xlim.fr; nicolas.bui@xlim.fr; christophe.guiffaut@xlim.fr).

Color versions of one or more figures in this article are available at <https://doi.org/10.1109/TEMC.2023.3259241>.

Digital Object Identifier 10.1109/TEMC.2023.3259241

To overcome the constraints of classical RCs (costly, not movable, requirement of a mode stirrer and its associated motor), a new kind of RCs has been proposed in the early 2000's, the so-called vibrating intrinsic reverberation chamber (VIRC) [7], [8]. It consists in a metallic tent whose vibrating movement ensures time-varying boundary conditions, thus avoiding to insert a rotating stirrer. This facility is assumed to be low cost (with respect to a conventional RC of same volume), presents the advantage to be installed (and uninstalled) in a limited amount of time and is, therefore, movable in order for instance to realize in situ tests.

In the field of numerical modeling, one understands that the simulation of a VIRC is somewhat difficult in reason first of the complex geometry of the metallized canvas at a given instant and second to its continuous movement all along the time. However, several attempts have been made in the past using the FDTD method and a staircase mesh of the tent [9]. First, Kouveliotis et al. [10], [11], [12] proposed to model the VIRC with a unique simulation considering successively a given number of different geometries. More recently, Hara et al. [13], [14] proposed to perform an analysis after the full simulation of several independent VIRC geometries. One can consider that the staircase mesh of the VIRC used in these studies does not respect the real time-varying shape of the metallized canvas. Moreover, the small-dipole antennas considered in these papers are quite basic and do not represent a real configuration used in RCs.

In this article (which is an extension of [15]), we are presenting the process we have implemented in order to simulate a VIRC with the FDTD method using for the first time (to the best of our knowledge) a conformal mesh [16], [17] in order to model a realistic VIRC geometry. Moreover, in order to reproduce as faithfully as possible a real experimental setup implemented in VIRC, the antenna considered in the simulations is a log-periodic one, an antenna typically used in RC. Finally, the process used to generate the VIRC geometry has been improved in order to take into account the movement of the canvas, i.e., the geometry of the VIRC generated for a given instant is dependent of the geometry considered at the previous instant. Performance of the simulated VIRC as a RC are, therefore, characterized (for various quality factors) using the “well-stirred (WS) condition” method [18], [19], [20], a method that has been used recently to characterize in both frequency and time domains the performance of a real VIRC [21].

The rest of this article is organized as follows. In Section II, each step of the process implemented to simulate a VIRC using

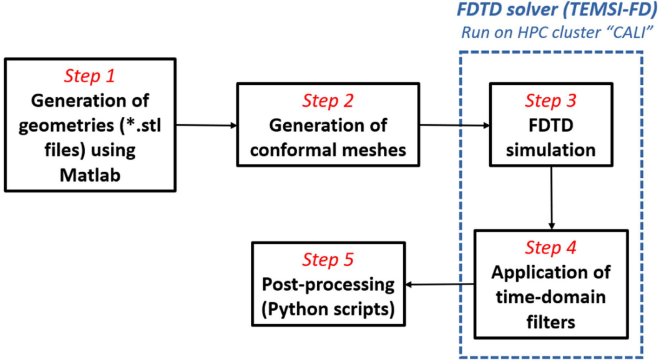


Fig. 1. Workflow illustrating the different steps of the simulation process.

an FDTD conformal mesh is detailed, from the generation of uncorrelated and correlated geometries to the application of losses during the postprocessing. Section III is devoted to the analysis of the results obtained first in the frequency domain for uncorrelated geometries and second in both frequency and time domains for correlated ones. It is shown in particular that the results obtained are perfectly in line with previous experimental results [21] that validates the relevance of the proposed simulation process. Finally, Section IV concludes this article.

II. PROCESS OF THE FDTD SIMULATIONS

All the simulations have been performed using the “TEMSI-FD” FDTD code developed in-house at the XLIM Laboratory. This solver implements the Yee scheme [9] and conformal techniques [22], [23], [24] to accurately model curved geometries. Conformal mesh generation is done with an associated preprocessing meshing tool. This software also implements several interesting features potentially helpful for VIRC simulations, such as oblique thin wire modeling [25] (for instance to model realistic antennas as shown later), several cable types and thin conducting plate models, as well as OpenMP/MPI parallelization.

Fig. 1 shows the workflow used in our simulation process, each step being detailed in the following sections.

A. Generation of the Geometries

1) *Uncorrelated Geometries*: In this article, for the sake of simplicity, we chose to implement a very simple but sufficiently efficient algorithm in order to test as a first step our complete simulation procedure (the generation of geometries matching the ones of a real VIRC being the matter for future works). For each face of the VIRC, a reference grid is generated with points spaced from each other with a distance s entitled the “grid step,” as shown in Fig. 2. The grid step can be seen as a kind of “correlation length” of a real canvas, meaning that the movements of two points of a real canvas spaced with a distance lower than the grid step are most of the time correlated.

Except for the points on the edges of the surface that are set to remain fixed, the new coordinates $x_n(i)$, $y_n(i)$, and $z_n(i)$ of an inner point of index i are computed randomly for the n th

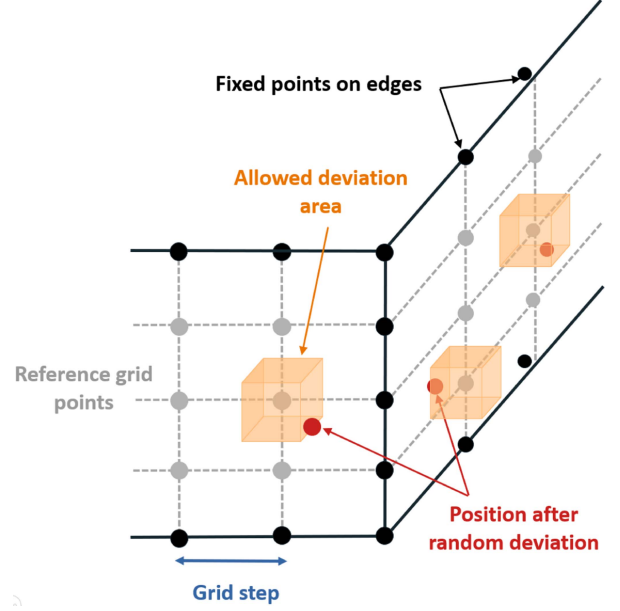


Fig. 2. Diagram explaining the process of the grid generation in the case of $k = 0.66$. Black points are stationary points located on the edges of the VIRC walls, whereas red ones are potentially moving. The cube shows (schematically) the possible area for the final position of the corresponding point after the random draw.

geometry using the following relations:

$$\begin{aligned}
 x_n(i) &= x_g(i) + s \cdot k \cdot r_1(n, i) \\
 y_n(i) &= y_g(i) + s \cdot k \cdot r_2(n, i) \\
 z_n(i) &= z_g(i) + s \cdot k \cdot r_3(n, i)
 \end{aligned} \tag{1}$$

where $x_g(i)$, $y_g(i)$, and $z_g(i)$ are the coordinates of the point in the reference grid, s is the grid step, k is an empirical coefficient between 0 and 1 related to the authorized movement in each of the three directions, and r_1 , r_2 , and r_3 (calculated for each geometry n and each point i) are random numbers (generated using a uniform distribution) included in the range between -0.5 and 0.5 . Therefore, even if k is 1, the process ensures that there is no overlapping between two adjacent points.

For each generated geometry of a VIRC (corresponding to the geometry of the VIRC at a given instant), a program computes the coordinates of each point and exports these information in a *stl* geometrical format file. Each square shown in Fig. 2 is discretized into two triangles along one of its diagonal. This file is then treated by our homemade conformal FDTD mesher.

2) *Correlated Geometries*: The creation of correlated geometries means that a given geometry depends on the previous one. After creating the first geometry with the process described in the previous section, the new coordinates $x_n(i)$, $y_n(i)$, and $z_n(i)$ of an inner point of index i for the n th geometry are computed randomly using the following relations:

$$\begin{aligned}
 x_n(i) &= x_{n-1}(i) + s \cdot k/d \cdot r_1(n, i) \\
 y_n(i) &= y_{n-1}(i) + s \cdot k/d \cdot r_2(n, i) \\
 z_n(i) &= z_{n-1}(i) + s \cdot k/d \cdot r_3(n, i)
 \end{aligned} \tag{2}$$

with $x_{n-1}(i)$, $y_{n-1}(i)$, and $z_{n-1}(i)$ the coordinates of the same point in the previous created geometry and d the division factor,

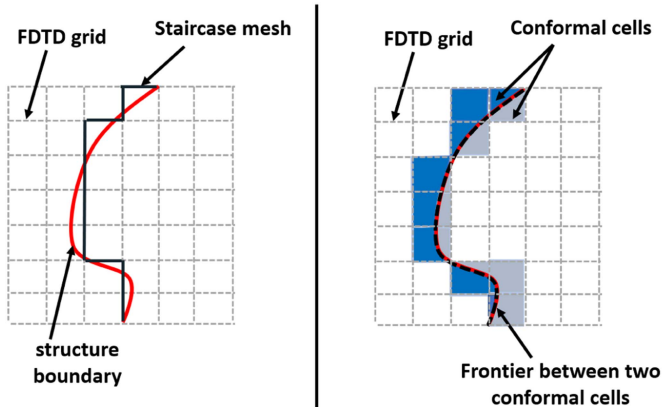


Fig. 3. Diagram explaining (in two dimensions) the difference between staircase mesh (on the left-hand side) where the real geometry of a curvilinear structure is not well respected and conformal mesh (on the right-hand side). Shaded cells are conformal cells (note that each shaded square contains in reality two conformal cells, one on each side of the curvilinear structure to mesh).

which is an integer greater than 1 (k and r being defined similarly as in the previous section). Therefore, the ratio k/d drives the authorized movement between two correlated geometries and ensures that the movement from two successive created geometries is smaller with respect to the movement between the reference grid and the first created geometrical (or between two uncorrelated geometries). It is worth noting that this algorithm is quite basic as the scope of this article is not to provide an excellent algorithm but more to prove that it is possible to simulate (for the first time) a realistic movement of the VIRC with FDTD conformal meshing. It has been observed that in some occasions (if the authorized movement between two successive geometries is too high and/or if the number of correlated geometries is too important but not in the examples shown in this article), some VIRC geometries may exhibit quite sharp peaks leading to conformal mesh problems, some conformal cells being too small.

B. Conformal FDTD Simulation

Conformal techniques [22], [23], [24] for the FDTD method are designed to reduce significantly staircase modeling errors. In cells crossed by conducting surfaces (i.e., the so-called “conformal cells”), the integral form of Maxwell–Faraday’s equation is applied on each face. Each free space face is a quadrilateral defining the contour path according to its four edges. A conformal cell is a free space region delimited by the structure boundary on at least one face and the free space regions on the other faces, as shown in two dimensions in Fig. 3. The structure boundaries are here considered as perfect electrical conductors (PEC), which means that no additional unknowns are required along this part of the contour path. Consequently, geometry data, such as edge lengths or cell areas, are required and computed during the mesh generation.

Our conformal mesher developed in-house for TEMSI-FD computes geometrical data from a tessellation (*stl* geometrical format) of the 3-D structure used as an input. Alternative approaches exist with some specificities, such as Junkin and Parron [16] computing additional edges inside a Yee cell, Waldschmidt and Taflove [26] working on finite element facets as inputs, Su

et al. [27] constructing polygons from the triangular patch intersections with a grid plane (which requires closed objects), and Benkler et al. [28] addressing models merging different ones.

All conceivable situations of PEC structure intersection can be encountered in conformal cells. Most of the time, a cell is splitted in two independent partitions but sometimes it may be splitted in several ones, for example, in the case of tee or cross shape. Conformal FDTD solving process is applied on each of them, which slightly increases the number of unknowns and the computational time. As conformal cells have variable sizes, small ones may become unstable for a given Courant–Friedrichs–Lewy (CFL) number.

Conformal techniques stabilize such cells, for example, in [22] and [24], by modifying locally the edge length or the cell area. Both techniques are of equivalent accuracy and are more accurate than the original one [29]. A CFL fixed around 0.5 is a good tradeoff between accuracy and solving efficiency. A fourth technique [23] called the enlarged cell technique is of second-order accuracy and can operate without restriction on the CFL. Unstable conformal region is also stabilized by enlarging virtually unstable cells toward stable adjacent cells. However, additional treatments reducing slightly the potential gain are required during the time iteration resolution of the problem. Moreover, some conformal unstable cells are really difficult to enlarge virtually. Consequently, these ones should be stabilized by increasing locally the conformal face area. This correction is stronger than the usual technique [22] due to the high CFL, which may lead to inaccurate local response of the EM field. Therefore, in this article, the conformal method used is a simplified version of [24].

After the conformal mesh generation process, FDTD simulations are run on a high-performance computing (HPC) machine (the CALI cluster equipped of Intel Xeon E5-2650 v2 processors).

C. Postprocessing for Insertion of Losses

Since the metallic walls constituting the VIRC are considered as perfect electrical conductors, the cavity losses are handled, in a specific postprocessing operation, after applying an exponential filter on output data. This method described in [30] has been proven to be experimentally relevant for RC simulations in [31].

The method consists in performing a “lossless” simulation during a “reasonable” observation time T , the term reasonable meaning that this time is insufficient to lead to a total attenuation of the field within the resonating structure. This is why the simulation is called (abusively) lossless because the only loss factor within the RC is the $50\ \Omega$ load connected to the antenna. When this simulation is over, the time domain response of any output signal designated by the term $U(t)$ (for instance the total electric field in one point) is multiplied by a time domain filter $f_Q(t)$ defined as follows:

$$f_Q(t) = e^{-\pi \cdot \Delta_f \cdot t} \quad (3)$$

where Δ_f is the “average mode bandwidth” [32] (also referred in the literature to the “coherence bandwidth”) related to the average composite quality factor $Q(f)$ of the cavity at a given frequency by the straightforward relationship $\Delta_f = f/Q(f)$.

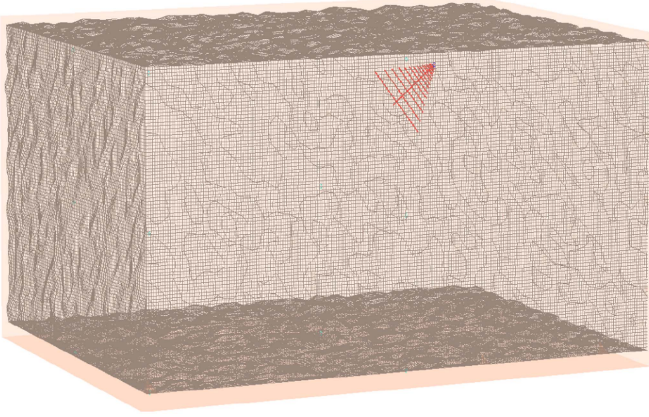


Fig. 4. Conformal mesh visualization of one geometry of a simulated VIRC and of the log-periodic antenna model inserted inside.

The obtained signal $U_f(t)$ obtained after the filtering process (see for instance [31, Fig. 3]) can, therefore, be expressed as follows:

$$U_f(t) = R_T(t) \cdot f_Q(t) \cdot U(t) \quad (4)$$

with $R_T(t)$ a rectangular window of duration T .

It is worth noting that this method presents the great advantage to allow various Δf values to be applied from only one lossless FDTD modeling, this without additional computation times. In these conditions, it is fundamental to verify that $U_f(t)$ tends toward zero for the smallest Δf value, i.e., when the applied losses are the smallest ones.

III. RESULTS

A. From Uncorrelated Geometries

1) *Description of the Simulations:* A VIRC model of dimensions $4.5 \text{ m} \times 3.5 \text{ m} \times 2 \text{ m}$ has first been meshed using the process described in Section II-A.1 (with the parameters $s = 10 \text{ cm}$ and $k = 0.4$) in order to obtain 50 different geometries, all these geometries being, therefore, uncorrelated. An example of created geometry is shown in Fig. 4.

The maximum frequency of the study is given by the dimension of the regular FDTD mesh size, which has been here set to 2 cm. Considering the common stability criterion of $\lambda/10$, it implies a maximum frequency f_{\max} of 1.5 GHz. The minimum frequency of the simulations is set to 100 MHz, in order to correctly observe the transition frequency range where the undermoded RC becomes sufficiently WS. The number of cells is, respectively, $239 \times 189 \times 114$ for each direction, which corresponds to roughly 5.15 millions of cells.

The simulated emitting antenna, also shown in Fig. 4, is a log-periodic antenna made with a collection of oblique thin wires [25] and designed to be satisfyingly matched on the whole bandwidth of interest. The antenna is located in one of the upper corner of the VIRC at a distance from the walls sufficiently large in terms of wavelengths. The antenna excitation is done using a Gaussian impulse signal combined with a sine wave modulation voltage source (of 50Ω internal impedance) centered on a bandwidth around 900 MHz.

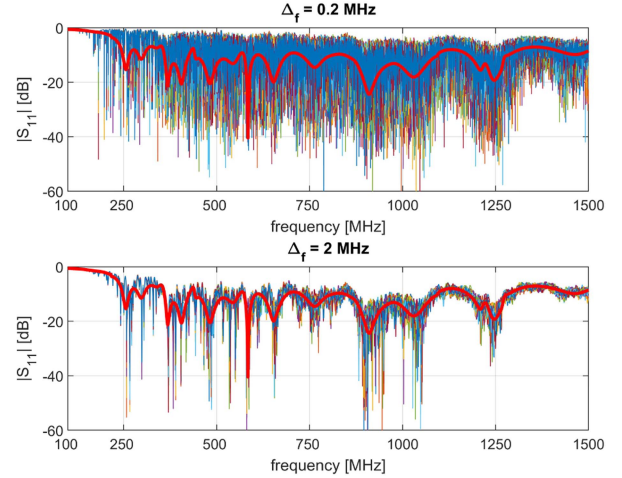


Fig. 5. Magnitude of S_{11} obtained for $N = 50$ uncorrelated geometries of the VIRC and for two values of Δf . Comparison with the same result calculated in free space (thick curve).

The output result of these simulations is the reflection coefficient parameter (i.e., S_{11}) of the antenna calculated for each generated geometry on the whole frequency range of interest. For each geometry, ten different values of Δf from 0.2 to 2 MHz (with a step of 0.2 MHz) have been considered.

2) *General RC Results:* The S_{11} magnitude of the antenna calculated on the bandwidth 0.2–1.5 GHz is shown in Fig. 5 for each created geometry and for two different values of the mode average bandwidth Δf (i.e., 0.2 and 1 MHz). It is particularly clear that the presented results look like experimental ones (see [21, Fig. 7]). First, the S_{11} parameter is heavily affected by the quality factor. Indeed, as often observed experimentally, the variations around the average value are larger for a higher Q (or a lower Δf). Second, it is observed that the reflection coefficient is close to 0 dB with extremely small variations in the lowest frequency band (i.e., below 200 MHz), which corresponds to the frequency range where the antenna is strongly unmatched, particularly within the RC. Indeed, it is difficult for the antenna to transmit any energy to the cavity in reason of the low modal density of the resonating enclosure.

From these S_{11} results, it is straightforward to compute and analyze the composite quality factor Q , which is a fundamental parameter driving the RC behavior. As demonstrated in [33], Q can be calculated from S -parameter measurements and particularly the S_{11} parameter using the following formula:

$$Q = \left\langle |S_{11} - \langle S_{11} \rangle|^2 \right\rangle \frac{Z_0 \cdot \omega \cdot \epsilon \cdot V}{(\lambda^2/4\pi) \left(1 - \langle |S_{11}|^2 \right) \eta^2} \quad (5)$$

where Z_0 is the wave impedance, ω the angular velocity, λ the wavelength, η the antenna efficiency, ϵ the vacuum permittivity, and V the RC total volume.

The results obtained using (5) for three different values of the Δf parameter are shown in Fig. 6. The total amount of losses in the RC are related first to the losses added with the time-domain filtering process as described previously but also in reason of the antenna losses (which is connected on a 50Ω load). The well-known Q -factor of an antenna (defined here Q_a) inserted

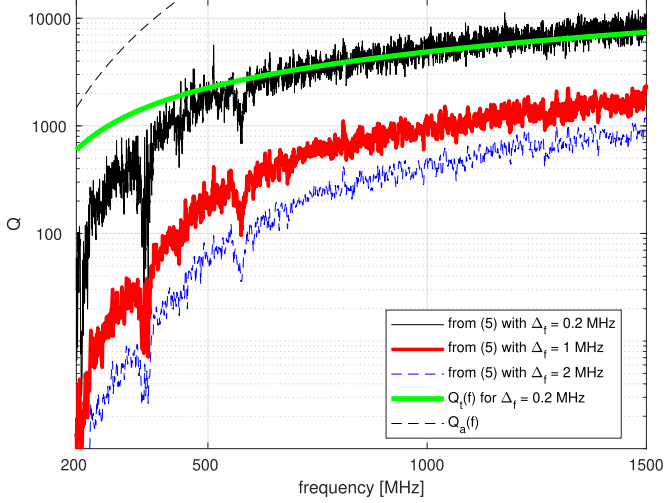


Fig. 6. Composite Q -factor calculated as a function of Δ_f .

in a RC writes

$$Q_a = 16\pi^2 \frac{V}{\lambda^3}. \quad (6)$$

Therefore, the theoretical Q -factor (called Q_t) we should obtain as a function of the frequency f can be expressed as follows:

$$Q_t(f) = \left(\frac{1}{Q_a(f)} + \frac{\Delta_f}{f} \right)^{-1}. \quad (7)$$

Fig. 6 presents also the theoretical $Q_t(f)$ we should obtain for $\Delta_f = 0.2$ MHz. Logically, this value matches pretty well the Q -factor obtained from the simulated results, particularly above 500 MHz. The discrepancy observed below 500 MHz cannot be attributed to $Q_a(f)$ (which is also plotted on the figure below 400 MHz) but more probably on the limit of (5) in the case of a strongly unmatched antenna (as shown in Fig. 5 in this frequency range).

3) *Verification of the WS Condition:* In this section, the aim is to analyze the performance of the simulated VIRC as a RC using the “WS condition method,” as this frequency-domain method has recently been extended to the case of VIRC [21].

The method is summarized here briefly (see [18], [19], and [20] for a complete description of the method). For each set of $N = 50$ simulations obtained for a given Δ_f value, the WS condition method is applied on S_{11} data calculated at each frequency, and more exactly on the stirred part of S_{11} , i.e., S_{11}^{sti} (which is computed after the removal of the S_{11} average at this frequency). The method investigates the ability of the RC to produce stirred contributions having properties matching the ones obtained in a WS RC. The complete definition of the WS condition given in [18] and [20] leads to consider that the assessment of both the EM field distributions and of the sample correlation are required to analyze the WS condition. They are, respectively, assessed thanks to the Anderson–Darling (AD) goodness-of-fit test [34] and to the first-order autocorrelation coefficient $r(1)$ [35]. Then, a polynomial curve fitting (PCF) allows two different frequencies f_1 (related to the EM field distributions) and f_2 (related to the EM sample correlation) to be

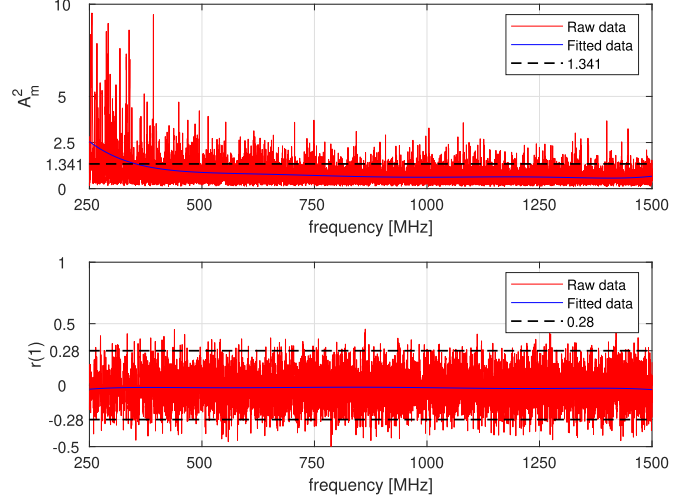


Fig. 7. Modified AD statistic A_m^2 and first-order autocorrelation coefficient $r(1)$ calculated from $N = 50$ uncorrelated geometries for $\Delta_f = 0.2$ MHz.

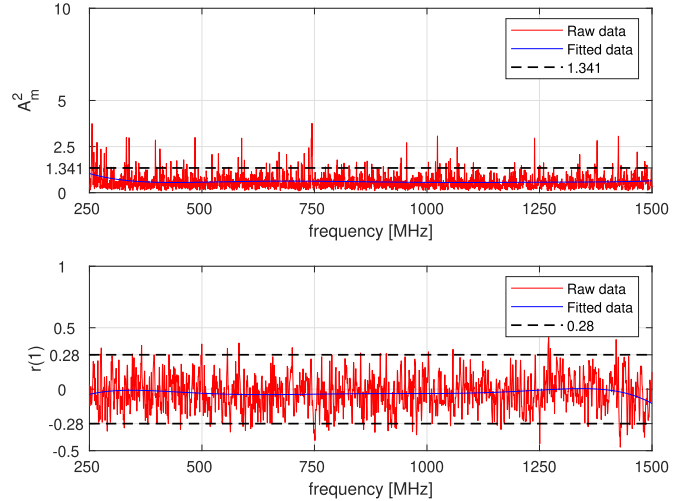


Fig. 8. Modified AD statistic A_m^2 and first-order autocorrelation coefficient $r(1)$ calculated from $N = 50$ uncorrelated geometries for $\Delta_f = 2$ MHz.

defined in order to know from which frequency each criteria is assumed to be respected. These frequencies are obtained when the PCF becomes lower than theoretically justified threshold values (respectively, 1.341 and 0.28 in the case of $N = 50$ considered geometries). The final output of the method, i.e., the frequency f_{wsc} , is the maximum of both frequencies in order to be sure that both criteria are matched above f_{wsc} .

Figs. 7 and 8 show the outputs of the WS condition method for two different values of Δ_f (note that the data obtained below 250 MHz have been excluded of the PCF computations). On the one hand, the analysis of the AD statistic (i.e., A_m^2) shows that the EM field distribution tends more rapidly toward the Rayleigh distribution in the lowest part of the frequency range when Δ_f increases, i.e., when the Q -factor decreases. On the other hand, the analysis of $r(1)$ shows, as expected, the absence of correlation on the whole frequency range of interest between all the generated geometries. All these results

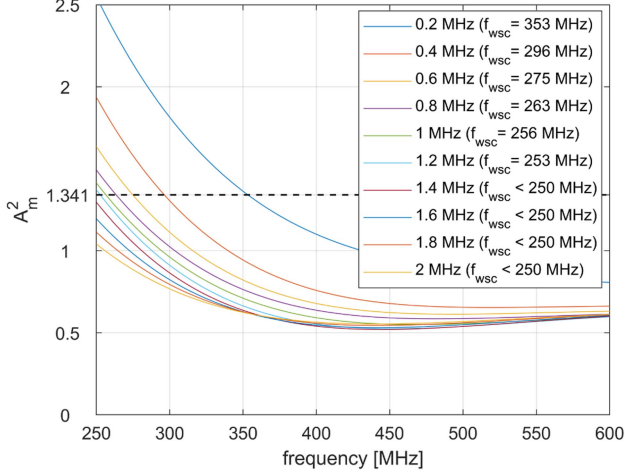


Fig. 9. Modified AD statistic A_m^2 as a function of Δ_f in the frequency range from 250 to 600 MHz. The value of f_{wsc} (i.e., f_1 here) is indicated in the legend for each Δ_f value.

match perfectly the conclusions previously drawn in [21] after analyzing VIRC measurements.

To go further, the polynomial curve fit of the AD statistic plotted in Fig. 9 for all the considered values of Δ_f clearly shows the influence of the Δ_f variation on the EM field distributions obtained in the VIRC (and also on f_{wsc} which is here f_1 , f_2 being not relevant as the results are perfectly uncorrelated).

Once again, the presented results in this subsection are highly similar to the experimental results obtained previously in VIRC (see [21, Figs. 9 and 10]).

B. From Correlated Geometries

For this new study, 500 correlated geometries using the process described in Section II-A.2 have been simulated in the frequency range 0.1 to 1 GHz (with the parameters $s = 10$ cm, $k = 0.4$, and $d = 15$). Indeed, considering the large number of correlated geometries that are generated, the maximum frequency of these simulations has been decreased in order to reduce the total computation times. The same ten values of Δ_f considered previously have again been considered in the results presented in this section.

Fig. 10 presents the magnitude of the S_{11} parameter of the emitting antenna calculated for each simulation at 0.25, 0.5, and 1 GHz for two values of Δ_f of 0.2 and 1 MHz. As it will be demonstrated later, the obtained results clearly show a correlation of the results, the S_{11} parameter obtained at a given instant being clearly dependent on the result obtained previously whatever the frequency. Moreover, as often observed in measurements, the variations of the S_{11} magnitude are larger when the frequency increases and also when the quality factor is higher (i.e., when Δ_f is lower).

To go further, we have calculated the autocorrelation coefficient $r(k)$ (k being the lag of the autocorrelation coefficient in terms of the simulation number) of the real part of the S_{11} parameter (assumed to be here $x(t)$) for the same frequencies

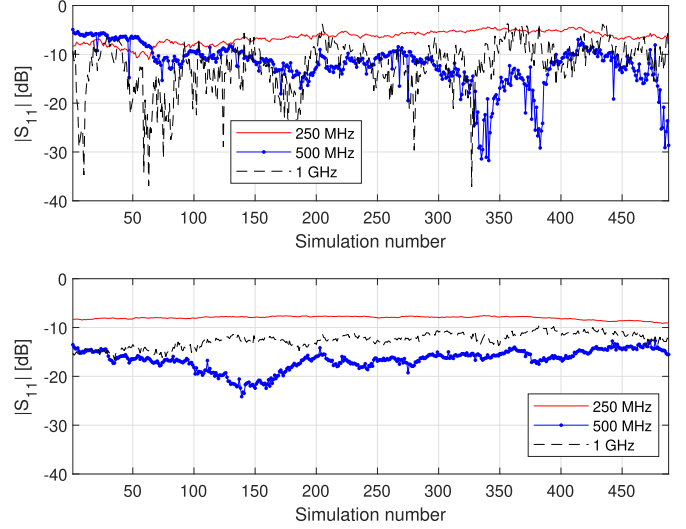


Fig. 10. Magnitude of the S_{11} parameter at three particular frequencies for each of the 500 correlated geometries and for $\Delta_f = 0.2$ MHz (top subplot) and $\Delta_f = 1$ MHz (bottom subplot).

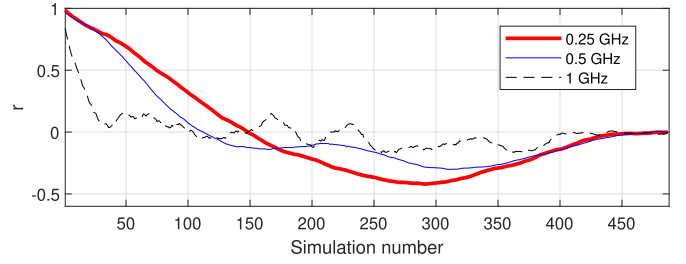


Fig. 11. Autocorrelation $r(k)$ of the real part of S_{11} calculated over the 500 correlated geometries at three particular frequencies for $\Delta_f = 0.2$ MHz.

using the following formula:

$$r(k) = \frac{\sum_{i=k+1}^N [x(i) - \langle x \rangle] \cdot [x(i-k) - \langle x \rangle]}{\sigma_x^2} \quad (8)$$

with σ_x the standard deviation of $x(t)$.

The autocorrelation coefficient $r(k)$ of the real part of S_{11} calculated over the 500 correlated geometries at the same three particular frequencies for $\Delta_f = 0.2$ MHz is shown in Fig. 11. Once again, the results are similar to experimental ones presented in [21]. It is in particular shown that the correlation is strong for the lower lag (in reason of the correlation of the generated geometries) but decreases rapidly and oscillates around 0.

To obtain a metric quantifying the lag leading to obtain two independent measurements, we have computed here the required lag k_u (called the “uncorrelated lag”) leading to an autocorrelation coefficient lower than the threshold value of 0.5 [21]. It is worth noting that this lag k_u could be easily converted in a time scale (similarly to the uncorrelation time t_u defined in [21]) after associating a time step δ_t between two successive simulations.

The uncorrelated lag k_u obtained each 10 MHz over the 500 correlated geometries is shown in Fig. 12 for $\Delta_f = 0.2$ MHz. In addition, to exhibit the general trend of k_u as a function of the frequency, a 25-MHz moving average filter has been applied on the results. It is shown that the uncorrelated lag

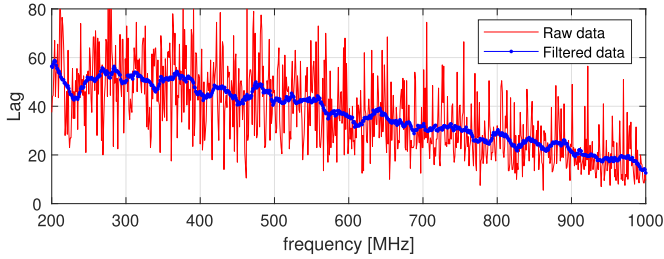


Fig. 12. Average of the uncorrelated lag k_u over the 500 correlated geometries for $\Delta_f = 0.2$ MHz (as well as a filtered result obtained with a 25 MHz moving average computation). To reduce the number of points of the curve, the results are shown with a 10-MHz step. Note that at each frequency, the uncorrelation lag considered is the average of the one obtained from the analysis of the real and of the imaginary parts of S_{11} .

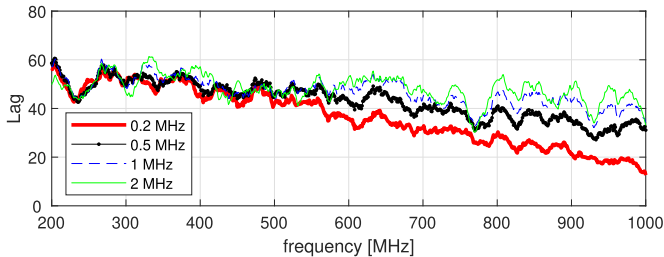


Fig. 13. Filtered uncorrelated lag k_u obtained for four different values of Δ_f and calculated over the 500 correlated geometries for frequencies shifted with a step of 10 MHz.

decreases with the frequency as it has already been observed in experiments [21].

To go further, the filtered uncorrelated lag k_u obtained as a function of frequency is shown in Fig. 13 for different Δ_f values. It is clearly shown that the uncorrelated lag increases with the value of Δ_f , and therefore when the Q -factor decreases. This, once again, confirms that the uncorrelation time in a VIRC increases when absorbers are inserted in.

C. About Computation Time

As already mentioned, the computations shown in this article have been performed on the CALI HPC cluster of the University of Limoges. At least, 15 simulations were able to run in parallel, each one of them being distributed on four processors. The average computation time for each of the 50 uncorrelated configurations considered in section III-A until 1.5 GHz was about 12 h per simulation. As the maximum frequency considered for the 500 correlated configurations was lower (i.e., 1 GHz), the average computation time has been reduced nearly to 2 h per simulation. Finally, with respect to an enclosure of similar volume simulated with a staircase mesh, the conformal FDTD simulation involves roughly a double computation time in reason of the CFL number used in our simulations (0.5 instead of 1 for staircase mesh).

IV. CONCLUSION

We have presented in this article a complete process allowing for the first time to model a VIRC using a conformal FDTD mesh in order to satisfyingly respect the geometry of the tent

at a given instant. The simulation of N uncorrelated VIRC has been proven to yield results similar than measurements in the frequency domain. Then, we have introduced a correlation between two successive geometries in order to represent a continuous movement of the canvas as a function of time. This led us to extract the “uncorrelation lag” of the VIRC as a function of the frequency and of the VIRC quality factor. The obtained simulated results have matched pretty well experimental ones previously published by some of the authors.

Future axis of work have already been identified. The canvas generation algorithm proposed in this article being quite basic, we will try in the future to propose processes that better respect the geometry of a real VIRC and its mechanical motion and then to compare experimental and numerical results. In parallel, conformal VIRC simulations makes possible to improve our physical understanding of a VIRC. For example, it will be interesting to study which are the type of canvas movements yielding to the best performance of the VIRC as a RC. Moreover, our homemade software and its conformal mesher can also simulate particularly well a “classical” parallelepipedic RC, including a conformal mesh of the mode stirrer. Then, it could be feasible to simulate the exact geometry of a RC and to compare computational results with the experimental ones after considering in the simulations the measured Q -factor of the RC.

ACKNOWLEDGMENT

This work was operated by the ANR, involving the XLIM Laboratory, CISTEME, and the “Jacques Dubois” company. The calculations presented in this article were carried out on the “CALI” high-power computing calculator of the University of Limoges, which was supported by the Limousin region, European Union, XLIM, IPAM, GEIST institutes, and University of Limoges.

REFERENCES

- [1] F. Moglie, “Convergence of the reverberation chambers to the equilibrium analyzed with the finite-difference time-domain algorithm,” *IEEE Trans. Electromagn. Compat.*, vol. 46, no. 3, pp. 469–476, Aug. 2004.
- [2] Y. Cui, G. Wei, S. Wang, L. Fan, and Y. Zhao, “Fast analysis of reverberation chamber using FDTD method and matrix pencil method with new criterion for determining the number of exponentially damped sinusoids,” *IEEE Trans. Electromagn. Compat.*, vol. 56, no. 3, pp. 510–519, Jun. 2014.
- [3] A. Coates, H. G. Sasse, D. E. Coleby, A. P. Duffy, and A. Orlandi, “Validation of a three-dimensional transmission line matrix (TLM) model implementation of a mode-stirred reverberation chamber,” *IEEE Trans. Electromagn. Compat.*, vol. 49, no. 4, pp. 734–744, Nov. 2007.
- [4] E. Amador, C. Lemoine, P. Besnier, and A. Laisné, “Reverberation chamber modeling based on image theory: Investigation in the pulse regime,” *IEEE Trans. Electromagn. Compat.*, vol. 52, no. 4, pp. 778–789, Nov. 2010.
- [5] H. Zhao and Z. Shen, “Efficient modeling of three-dimensional reverberation chambers using hybrid discrete singular convolution-method of moments,” *IEEE Trans. Antennas Propag.*, vol. 59, no. 8, pp. 2943–2953, Aug. 2011.
- [6] M. E. Gruber and T. F. Eibert, “A cavity green’s function boundary element method with spectral domain acceleration for modeling of reverberation chambers,” *IEEE Trans. Electromagn. Compat.*, vol. 56, no. 6, pp. 1466–1473, Dec. 2014.
- [7] F. Leferink, “Test chamber,” Patent NL-1010745, 1998.
- [8] F. Leferink, J. C. Boudenot, and W. van Etten, “Experimental results obtained in the vibrating intrinsic reverberation chamber,” in *Proc. IEEE Int. Symp. Electromagn. Compat. Symp. Rec.*, 2000, pp. 639–644.

- [9] K. Yee, "Numerical solution of initial boundary value problems involving Maxwell's equations in isotropic media," *IEEE Trans. Antennas Propag.*, vol. 14, no. 3, pp. 302–307, May 1966.
- [10] N. K. Kouveliotes, P. T. Trakadas, and C. N. Capsalis, "Examination of field uniformity in vibrating intrinsic reverberation chamber using the FDTD method," *Electron. Lett.*, vol. 38, no. 3, pp. 109–110, Jan. 2002.
- [11] N. K. Kouveliotes, P. T. Trakadas, and C. N. Capsalis, "FDTD calculation of quality factor of vibrating intrinsic reverberation chamber," *Electron. Lett.*, vol. 38, no. 16, pp. 861–862, Aug. 2002.
- [12] N. K. Kouveliotes, P. T. Trakadas, and C. N. Capsalis, "FDTD modeling of a vibrating intrinsic reverberation chamber," *Prog. Electromagn. Res.*, vol. 39, no. 3, pp. 47–59, 2003.
- [13] M. Hara, Y. Takahashi, R. Vogt-Ardatjew, and F. Leferink, "Validation of vibrating intrinsic reverberation chamber using computational electromagnetics," in *Proc. Joint Int. Symp. Electromagn. Compat. Sapporo Asia-Pacific Int. Symp. Electromagn. Compat.*, 2019, pp. 593–596.
- [14] M. Hara, T. Yoshikai, Y. Takahashi, R. Vogt-Ardatjew, and F. Leferink, "Numerical analysis of vibrating intrinsic reverberation chamber between various shielding effectiveness measurement techniques," in *Proc. Int. Symp. Electromagn. Compat.*, 2020, pp. 1–6.
- [15] F. Mahiddini, G. Andrieu, C. Guiffaut, and N. Bui, "Conformal FDTD simulation of vibrating intrinsic reverberation chambers," in *Proc. Int. Symp. Electromagn. Compat.*, 2022, pp. 345–348.
- [16] G. Junkin and J. Parron, "A robust 3D mesh generator for the Dey-Mitra conformal FDTD algorithm," in *Proc. 2nd Eur. Conf. Antennas Propag.*, 2007, pp. 1–6.
- [17] N. Bui, C. Guiffaut, and A. Reineix, "Field interpolation with generalized barycentric coordinates in conformal FDTD schemes," in *Proc. IEEE Int. Symp. Antennas Propag. USNC-URSI Radio Sci. Meeting*, 2019, pp. 1651–1652.
- [18] G. Andrieu, N. Ticaud, F. Lescoat, and L. Trougnou, "Fast and accurate assessment of the "well stirred condition" of a reverberation chamber from S_{11} measurements," *IEEE Trans. Electromagn. Compat.*, vol. 61, no. 4, pp. 974–982, Aug. 2019.
- [19] G. Andrieu and N. Ticaud, "Performance comparison and critical examination of the most popular stirring techniques in reverberation chambers using the "well-stirred" condition method," *IEEE Trans. Electromagn. Compat.*, vol. 62, no. 1, pp. 3–15, Feb. 2020.
- [20] G. Andrieu, *Electromagnetic Reverberation Chambers - Recent Advances and Innovative Applications*. Stevenage, U.K.: Inst. Eng. Technol., 2021.
- [21] G. Andrieu, N. Meddeb, C. Jullien, and N. Ticaud, "Complete framework for frequency and time-domain performance assessment of vibrating intrinsic reverberation chambers," *IEEE Trans. Electromagn. Compat.*, vol. 62, no. 5, pp. 1911–1920, Oct. 2020.
- [22] S. Benkler, N. Chavannes, and N. Kuster, "A new 3-D conformal PEC FDTD scheme with user-defined geometric precision and derived stability criterion," *IEEE Trans. Antennas Propag.*, vol. 54, no. 6, pp. 1843–1849, Jun. 2006.
- [23] T. Xiao and Q. H. Liu, "A 3-D enlarged cell technique (ECT) for the conformal FDTD method," *IEEE Trans. Antennas Propag.*, vol. 56, no. 3, pp. 765–773, Mar. 2008.
- [24] I. Zagorodnov, R. Schuhmann, and T. Weiland, "Conformal FDTD-methods to avoid time step reduction with and without cell enlargement," *J. Comput. Phys.*, vol. 225, no. 2, pp. 1493–1507, 2007.
- [25] C. Guiffaut, A. Reineix, and B. Pecqueux, "New oblique thin wire formalism in the FDTD method with multiwire junctions," *IEEE Trans. Antennas Propag.*, vol. 60, no. 3, pp. 1458–1466, Mar. 2012.
- [26] G. Waldschmidt and A. Taflove, "Three-dimensional CAD-based mesh generator for the Dey-Mitra conformal FDTD algorithm," *IEEE Trans. Antennas Propag.*, vol. 52, no. 7, pp. 1658–1664, Jul. 2004.
- [27] T. Su, Y. Liu, W. Yu, and R. Mittra, "A conformal mesh-generating technique for the conformal finite-difference time-domain (CFDTD) method," *IEEE Antennas Propag. Mag.*, vol. 46, no. 1, pp. 37–49, Feb. 2004.
- [28] S. Benkler, N. Chavannes, and N. Kuster, "Mastering conformal meshing for complex CAD-based C-FDTD simulations," *IEEE Antennas Propag. Mag.*, vol. 50, no. 2, pp. 45–57, Apr. 2008.
- [29] S. Dey and R. Mittra, "A locally conformal finite-difference time-domain (FDTD) algorithm for modeling three-dimensional perfectly conducting objects," *IEEE Microw. Guided Wave Lett.*, vol. 7, no. 9, pp. 273–275, Sep. 1997.
- [30] P. Bonnet, R. Vernet, S. Girard, and F. Paladian, "FDTD modelling of reverberation chamber," *Electron. Lett.*, vol. 41, no. 20, pp. 1101–1102, Sep. 2005.
- [31] A. Adardour, G. Andrieu, and A. Reineix, "On the low-frequency optimization of reverberation chambers," *IEEE Trans. Electromagn. Compat.*, vol. 56, no. 2, pp. 266–275, Apr. 2014.
- [32] P. S. Kildal, X. Chen, C. Orlenius, M. Franzen, and C. S. L. Patane, "Characterization of reverberation chambers for OTA measurements of wireless devices: Physical formulations of channel matrix and new uncertainty formula," *IEEE Trans. Antennas Propag.*, vol. 60, no. 8, pp. 3875–3891, Aug. 2012.
- [33] P. Besnier, C. Lemoine, and J. Sol, "Various estimations of composite Q -factor with antennas in a reverberation chamber," in *Proc. IEEE Int. Symp. Electromagn. Compat.*, 2015, pp. 1223–1227.
- [34] C. Lemoine, P. Besnier, and M. Drissi, "Investigation of reverberation chamber measurements through high-power goodness-of-fit tests," *IEEE Trans. Electromagn. Compat.*, vol. 49, no. 4, pp. 745–755, Nov. 2007.
- [35] O. Lundén and M. Bäckström, "Stirrer efficiency in FOA reverberation chambers. evaluation of correlation coefficients and chi-squared tests," in *Proc. IEEE Int. Symp. Electromagn. Compat. Symp. Rec.*, 2000, pp. 11–16.



Florian Mahiddini received the master's degree in engineering physics from Polytech Clermont-Ferrand, Aubière, France, in 2014, and the Ph.D. degree in physics from ISAE-SUPAERO, Toulouse, France, in collaboration with ONERA, Toulouse, France, in 2018.

In 2021, he was a Postdoctoral Fellow with the XLIM Laboratory, Limoges, France. He is currently a Research Fellow with the University of Strathclyde, Glasgow, U.K. His research focuses on the development of numerical models devoted to the electromagnetic characterization of electrical wiring interconnection systems.



Guillaume Andrieu (Senior Member, IEEE) was born in Limoges, France, in 1980. He received the master's degree in radio frequencies and optical communications from the University of Limoges, Limoges, France, in 2003, and the Ph.D. degree in electronics from the IEMN Laboratory, Telice Group, University of Lille, Lille, France, in 2006.

In 2003, he joined the Renault Technocentre, Guyancourt, France. In 2006, he joined the XLIM Laboratory, University of Limoges, as a Postdoctoral Fellow, where he has been an Associate Professor since 2009. His current research interests include coupling on cables and electromagnetic compatibility testing, including reverberation chambers and bulk current injection tests.



Nicolas Bui was born in Nantes, France, in 1989. He received the master's degree in mathematics and applications from the University of Nantes, Nantes, France, in 2012, and the Ph.D. degree in electronics from the University of Limoges, Limoges, France, in 2016.

Since 2017, he has been with XLIM Laboratory, University of Limoges, as a Postdoctoral Scientist. His research focuses on the development of numerical methods in the time domain for applications in electromagnetic compatibility and scattering.



Christophe Guiffaut (Member, IEEE) was born on 14 March, 1973, in Chateaubriant, France. He received the master's and Ph.D. degrees in electronics and telecommunications from the University of Rennes, Rennes, France, in 1997 and 2000, respectively.

In 2002, he joined the CNRS Research Center, Paris, France, and in 2002, he integrated with the XLIM Laboratory, University of Limoges, Limoges, France. His research interests include the numerical methods in the time domain with various application areas, such as EMC and radar, numerical modeling developments concern cables, lightning and HIRF effects on aircraft and building, antennas, metamaterials, radar cross-sectional computing, and ground penetrating radar.